Benefits of Using Rapid Microwave Heating in the Synthesis of Metal-free Carbon Electrocatalysts

Kodai Satoh[‡], *Takumi Odawara*[‡], *Yusaku Yamazaki*[‡], *Takatoshi Murakami*[‡], *Hironobu Ono*[‖], *Shinichiroh Iwamura*[§,†], *Shin R. Mukai*[§], *Isao Ogino*[§*]

AUTHOR ADDRESS.

[‡] Graduate School of Chemical Sciences and Engineering, Hokkaido University, Sapporo, Hokkaido 060-8628, Japan

[‖] Nippon Shokubai Co. Ltd., Suita, Osaka 564-0034, Japan

[§] Faculty of Engineering, Hokkaido University, Sapporo, Hokkaido 060-8628, Japan

KEYWORDS. Metal-free catalyst, heteroatom doped catalyst, electrocatalyst, reactive microenvironment, topological defect, pore hydrophobicity

ABSTRACT

Heat treatment constitutes a key synthesis step for nitrogen-doped carbons, which have been investigated for applications to numerous electro- and thermo-catalytic reactions. However, the conventional approach relying on bulk heating limits our ability to tailor catalysts' properties due to the fast gasification of carbon-based materials in reactive atmospheres such as NH_3. In this paper, we report the advantages of utilizing microwave technology for improving the catalytic performance of nitrogen-doped carbon via selective and rapid heating. We synthesized two distinct sets of nitrogen-doped carbons from graphene oxide: one exhibiting micropores approximately 1 nm in width (**HS**) and another characterized by their scarcity of micropores (**NS**). Despite their comparable nitrogen contents, **HS** exhibits significantly higher activity than **NS** in the electrochemical oxygen reduction reaction (ORR) in an acidic electrolyte. These samples underwent further heat treatment in NH_3 or N_2 using a conventional tubular furnace or a single-mode microwave reactor apparatus. Our results demonstrate that microwave heating limits the gasification of carbon-based materials, which effectively permits heating up to an average temperature of 1400 ºC in NH_3. Microwave heating of **HS** in NH_3 enhances its pore hydrophobicity while maintaining microporosity, substantially improving ORR activity. Conversely, microwave heating of **HS** in N_2 considerably diminishes its ORR activity despite enhancing pore hydrophobicity and maintaining an adequate nitrogen species presence. These findings emphasize the crucial role played by the coexistence of carbon defects and specific nitrogen sites generated through heating in an NH_3 atmosphere within hydrophobic micropores for high ORR activity. In summary, our data highlight the distinct advantages of high-temperature treatment of nitrogen-doped carbons in NH_3 using microwave heating. This approach enables us to adjust the reactive microenvironments, thereby improving catalytic performance without sacrificing crucial active sites within micropores for ORR catalysis.

INTRODUCTION

Nitrogen-doped carbons have emerged as promising metal-free electrocatalysts for applications such as oxygen reduction reaction (ORR) in hydrogen fuel cells.[1–11] They can also be used as catalyst supports for atomically dispersed metals for various electro- and thermo-catalytic processes, as specific doped nitrogen sites act as anchoring sites for metal atoms[12–16] and metal nanoparticles.[17–21] Nitrogen-doped carbons are commonly synthesized by pyrolyzing a mixture of carbon and nitrogen precursors under an inert atmosphere, typically at temperatures ranging from 600 to 1100 ºC. A second method involves introducing oxygen functional groups onto a carbon material using strong acids, followed by heating in NH_3 to incorporate nitrogen species through a reaction with the oxygen functional groups.[22–25] The heat treatment is crucial in the synthesis of these materials as it impacts the type and concentration of heteroatom dopants, [23,25,26] structural defects,[27,28] π-electron delocalization and associated Lewis basicity,[29] acid-base properties,[25,30] electrical properties,[24,31] surface polarity, and porosity of the materials. However, traditional methods of heating, which rely on bulk heating, have limitations when it comes to tuning the desired properties of carbon materials. For example, recent studies on electrochemical reduction of O_2 or CO_2 indicate the general significance of high electron conductivity and pore hydrophobicity for carbon-based electrocatalysts.[32,33] One way to achieve this goal involves subjecting the carbon material to heat treatment above 1100 ºC.[34,35] However, this process unavoidably eliminates the necessary nitrogen dopants and carbon defects as well.[26] An alternative is to heat the carbon material in the presence of NH_3. This process can help incorporate the nitrogen species in the carbon, as demonstrated in the synthesis of nitrogen-doped carbon nanotubes.[36] Additionally, the reductive nature of NH_3 can aid in the removal of oxygen species.[24] However, a challenge arises with NH_3 decomposition occurring above 800 ºC, which generate radicals such as $NH\cdot$ and $NH_2\cdot$ that cause gasification of carbon to methane and cyanogen species (e.g. $C + NH_3 \rightarrow HCN + H_2$,).[37,38] Nevertheless, the selective gasification of the amorphous, oxygen-rich domain of the carbon by NH_3 has the potential to improve catalyst performance by creating sites with increased basicity inside micropores, as reported in the context of atomically dispersed supported iron catalysts.[39-42] However, this process also limits the temperature range that can be used due to the substantial gasification that occurs. For example, when carbon black powders were heated in a gas stream of $NH_3/H_2/Ar$, the rate at which carbon materials loses weight increased exponentially

with an apparent activation energy of 230 kJ mol^{-1}, reaching more than 100% per hour at 1000 ºC.[43] The rate-vs.-temperature data reported in the literature suggests that heat treatment above 1100 ºC is impossible. A graphite material exhibited a lower rate of weight loss than carbon black materials due to higher crystallinity. However, it limits the amount of nitrogen atoms that can be incorporated into the material to below 0.4 atomic%, as determined by X-ray photoelectron spectroscopy (XPS).[43] Conventional heating in an electrically heated furnace relies on conduction, advection, and radiation to transfer thermal energy to a sample. The Joule effect creates thermal energy in the furnace wall, which is then transferred to the sample via a gas. This approach inevitably heats NH_3, which facilitates its decomposition and leads to excessive gasification of carbon at high temperatures.

The goal of this research is to investigate the potentials of the microwave heating for synthesis of nitrogen-doped carbon catalysts. Microwaves can selectively, directly, and rapidly heat carbon materials,[44] while the surrounding gas is at significantly lower temperatures.[45] Therefore, we postulated that microwave heating minimizes the gasification of carbon materials in the presence of NH_3 above 1100 ºC while they are being doped with N species and retain carbon defects necessary for catalysis. We substantiate the proof-of-concept of this work through comparative experiments using both microwave and conventional heating methods. Importantly, our work highlights the favorable impacts of short microwave heating in NH_3 on tuning reactive microenvironment in nitrogen-doped carbon, improving the catalytic performance for the electrochemical oxygen reduction reaction in an acidic electrolyte.

METHODS

Synthesis of Catalysts. *Synthesis of Reduced Graphene Oxide (GO) Samples.* Three reduced GO samples were synthesized for the second heat treatment as shown in Scheme S1 in the Supporting Information. Two of them were obtained from Nippon Shokubai where GO had been reduced in the liquid-phase using L-ascorbic acid. These samples were denoted as denoted as **NS1** and **NS2**. The morphology of these samples is shown in Figure S1 in the Supporting Information. The third sample, labeled as **HS**, was prepared via a two-step method as follows: First, a GO dispersion was prepared by combining 84 g of a GO slurry (Nippon Shokubai, 2.0 wt%, lot number = AX-1-FN-W-212) with 36 mL of an aqueous ammonium hydroxide solution

(NH_4OH, 25 wt%) in a 250-mL polyethylene bottle. The suspension was stirred thoroughly at room temperature and then divided into three portions. Each portion, with a pH of approximately 11.6, was transferred within a Teflon-lined stainless autoclave (Parr instruments, 45 cm^3). The slurries were sealed in the autoclaves and subjected to autogenous pressure heating at 180 ºC for 12 h without stirring in a forced-convection oven. This process yields a monolith sample by reducing the GO and doping it with some nitrogen species simultaneously. After cooling to room temperature, the resultant monolith sample was recovered by decantation and treated with five washing-decantation cycles with *t*-butyl alcohol (TBA) to replace water with TBA. After freeze drying at –10 ºC, the monolith sample (≈1.4 cm in diameter and ≈4 cm in length) was heated at 1000 ºC for 3 h in a tube furnace in a flow of N_2 (99.99%). The final products were typically obtained with a solid yield of 53 wt%. The monolith sample (Figure S2 in the Supporting Information) was cut into small particles (<1mm) for the heat treatment described in the next section.

Conventional Heating. Heat treatments of the initial GO-derived samples were performed in a tubular quartz reactor shown in Figure S3 in the Supporting Information. Approximately 20 mg of sample (particle sizes <1 mm) was loaded in a combustion boat (11 cm long and 1 cm high) and placed into the reactor (1 in. OD and 65 cm length). The reactor was then mounted horizontally in a single-zone furnace (Asahi Rika, ARF-30K, 500 W) and connected to the feed gas line through a 1 in. Swagelok Ultra-torr fitting. The reactor was purged with a 40 mL min^{-1} NH_3 gas (Sumitomo Seika, 99.9%) for 20 min. The reactor temperature was controlled using the furnace, which was equipped with a Shimaden DSS83 controller and a K-type thermocouple attached to the periphery of the reactor wall. Samples were heated to a specified temperature (*T*) between 800 and 1100 ºC at a ramp rate of 10 ºC min^{-1}. After 5 min at the target temperature, the furnace was cooled to room temperature naturally, without opening it, and still under flowing NH_3. The reactor was then purged with N_2 at room temperature for 10 min. The treated samples were removed from the reactor and weighed to calculate the yield. Samples were denoted **HS-CH*T*** and **NS1-CH*T*** or **NS2-CH*T***, where ***T*** stands for treatment temperature.

Microwave heating. Heat treatments by microwave were performed in a microwave apparatus shown in Figure 1. The apparatus consists of a Wattsine WSPS-2450-1500 microwave generator (maximum power

output of 1.5 kW, 2.45 GHz solid-state generator), an iris, a manual 3-stub tuner, an Agilent E4418B power meter, and a rectangular-shaped monomodal cavity. Approximately 20 mg of GO sample was loaded on a frit located in the center of a microwave-transparent quartz-walled reactor (1 cm O.D., 50 cm long). The reactor was mounted vertically within the cylindrical cavity and sealed to the feed gas line using a Cajon fitting. NH_3 gas (99.9%) was metered using a mass flow controller (KOFLOC, model #3660) and fed from the bottom of the reactor at 15 mL min^{-1}. The temperature of the surface of sample bed was monitored by a quartz-transparent infrared (IR) thermometer (TMHXSTM0050, Japan Sensor Co.) through a viewing port and controlled by adjusting the output power of the microwave generator. The temperature calibration was performed in a conventional electrical furnace (Asahi Rika, ARF-30K) using samples before and after microwave treatments because of possible changes in dielectric properties as shown in Figure S4 in the Supporting Information. Typical emissivity values for samples before and after microwave treatments were 0.89 and 0.83, respectively. During the microwave heating, the positions of the 3-stub tuner and the sliding short plunger were routinely adjusted to place samples at the nodal position where the electric field reached a maximum and to minimize the microwave power reflected back beyond the iris. Upon microwave irradiation, the temperature of the sample bed was rapidly raised to the specified temperature. The reduced GO samples were then subjected to continuous microwave irradiation at the designated temperature (*T*) in flowing NH_3 or N_2 for 5 min. Afterward, the irradiation was stopped, allowing the samples to cool down naturally to room temperature. Finally, the inlet gas was switched to N_2 to purge the reactor. A typical temperature profile is shown in Figure S5 in the Supporting Information. Samples treated in NH_3 were designated as **HS-MW*T*-NH_3**, **NS1-MW*T*-NH_3**, or **NS2-MW*T*-NH_3**. Similarly, samples treated in N_2 were labeled by substituting **-NH_3** with **-N_2**.

Characterization of Catalysts. *N_2 Physisorption.* N_2 physisorption isotherms were measured at −196 ºC on a MicrotracBEL BELSORP-max. Before measuring isotherms, approximately 20 mg for **HS** and 30 mg for **NS** of powder sample was placed in a pre-weighed analysis tube and degassed under vacuum by heating to 250 ºC for 4 h. After degassing, the analysis tubes were cooled to ambient temperature, filled with inert gas, and capped to prevent the intrusion of air and moisture during transfer. Afterward, the analysis tubes containing activated samples, were weighed on an electrical balance to determine the mass of samples.

Subsequently, the tube was returned to the analysis port of the instrument. For each isotherm, warm and cold free space correction measurements were performed using helium gas (99.999%). N_2 isotherm data were recorded using N_2 gas (99.999%). Targeted relative pressures ranged from 10^{-8} to 0.98, and limits of excess and allowance dosing amounts were typically set to 5 and 10 $cm^3\ g^{-1}$, respectively. The isotherm data points were considered equilibrated when a pressure change of ≤0.3% occurred over an interval of 400 s. Specific surface areas were calculated using the Brunauer-Emmett-Teller (BET) model.

H_2O Vapor Adsorption. Vapor-phase H_2O adsorption isotherms were measured at 25 ºC using a MicrotracBEL BELSORP-max-12-N-VP instrument. Samples (~10 mg) were degassed by heating to 250 ºC for 4 h under a dynamic vacuum prior to measurements. Deionized water was subjected to three freeze-pump-thaw cycles.

Raman Spectroscopy. Raman spectra were acquired on a Renishaw inVia Reflex Raman microscope equipped with a 532-nm laser excitation source, a 20× objective, and a CCD detector. The diameter of the laser spot on the sample surface was a few micrometers at 20× objective magnification. The data were collected by point-by-point mapping with at least 50 different locations, selecting 10 points per ≈1mm-size particle for five particles. The incident laser power was <5 mW, and the illumination time was 10 s to avoid sample damage. A representative spectrum is provided for each sample. For analysis, each spectrum was deconvoluted, as reported in the literature,[46] into four Lorentzian peaks centered around ~1350 cm^{-1} (D_1), ~1620 cm^{-1} (D_2), ~1200 cm^{-1} (D_4), ~1580 cm^{-1} (G), and one Gaussian peak centered around ~1500 cm^{-1} (D_3) using the OriginPro software.

X-ray Photoelectron Spectroscopy. X-ray photoelectron spectroscopy (XPS) data were conducted on a JEOL JPS-9200 photoelectron spectrometer using a monochromatic Mg Kα X-ray source (1254.6 eV), generated from an electron beam operated at 10 kV and 10 mA. Samples for analysis were prepared by pressing the finely ground powders on indium foil (Niraco, 99.99%, catalog # IN-203260). To suppress sample charging during analysis, an electron and an ion neutralizer were operated simultaneously. The residual pressure during measurements was below 10^{-6} Pa. The spot size was approximately 3 μm. All spectra were calibrated according to the carbon peak at 284.8 eV. The obtained spectra were analyzed using the SPECSURF

analysis software. In particular, for the N1s spectra, the chemical species of pyridinic nitrogen (398.5 eV), pyrrolic nitrogen (400.1 eV), graphitic nitrogen (401.1 eV) were fitted with Gauss-Lorentz functions.

Boehm-type titration. Titration experiments were carried out with a set of aqueous stock solutions with pH spanning a pH range of approximately 1 to 11. These solutions were prepared by combining 0.1 M H_2SO_4 and 0.1 M KOH solutions. For each solution, an aliquot of 500 μL was taken, and its initial pH was measured using a HORIBA Micro ToupH electrode. Afterwards, 1 mg of dry nitrogen-doped catalyst was introduced to each solution, and the final pH was measured after 20 min of stirring.

Oxygen Reduction Catalysis. RDE Preparation. Electrochemical rotating disk electrode (RDE) experiments were carried out in a standard three-electrode cell (BAS, #012632) using a BAS RRDE-3A apparatus interfaced with a HOKUTO HZ-Pro potentiostat. The counter electrode was a Pt wire (Niraco, #351265), and the reference electrode was an Ag/AgCl saturated with KCl aqueous solution (BAS, model #013691). All potentials were referenced with respect to reversible hydrogen electrode (RHE), which were converted using the equation of $E_{RHE} = E_{Ag/AgCl} + 0.0591 \times pH + 0.197$ (V). The working electrode was a 5 mm ϕ glassy carbon disk electrode in PEEK sheath (BAS, #013482, geometric area of disk = 0.196 cm^2) for RDE. Before electrochemical measurements, the electrode surfaces were polished using paste (Al_2O_3 slurry; 0.05 μm) on a wet polishing pad (BASi, MF-1040) and rinsed with water to obtain a mirror-like finish. Prior to the preparation of catalyst ink, all catalyst samples were sieved to <600 μm and dried under vacuum at 80 ºC for at least 12 h in an oven. The catalyst ink was prepared by blending 2.5 mg of catalyst, 25 μL of 5% Nafion suspension in alcohol (Sigma-Aldrich, product No. 527084), 300 μL of deionized and distilled water, and 300 μL of ethanol (Wako, 99.5% purity) in an Eppendorf tube (AS ONE, 1-7521-01). The suspension was ultrasonicated in an ice bath for 30 min before loading a portion of it on the glassy carbon electrode (16 μL) while it was rotated at 700 rpm on a BAS RRDE apparatus to ensure homogeneous catalyst loading. The calculated loadings of catalyst were 0.325 mg cm^{-2} for RDE measurements.

Electrochemical Measurements. The ORR activity data were collected in an O_2-saturated 0.5 M H_2SO_4 aqueous solution (Sigma Aldrich, 28-5940-5). The catalyst coated on the electrode was activated by performing 20 cyclic voltammetry (CV) scans in N_2-saturated electrolyte at a scan rate of 50 mV s^{-1} and in

the potential range from 0.0 to 1.2 V vs. RHE until a reproducible CV was obtained. Linear sweep voltammograms (LSVs) were then recorded at a scan rate of 1 mV s^{-1}, starting at 1.1 V vs. RHE to –0.1 V. RHE, using a 0.02 V step and a potential hold time of 10 s, under a constant rate of 1700 rpm. A background measurement was performed in N_2-saturated 0.5 M H_2SO_4, and the data were subtracted to eliminate the pseudo-capacitance current and determine the current arising from ORR. ORR performance was evaluated by comparing the potential at a background-subtracted current density of −0.1 mA/cm^2. Tafel slopes were extracted by a linear regression analysis of the linear region near the onset potential, E_{onset}, in the Tafel plots acquired using RDE.

$$\text{Tafel slope} = -dE/d\ln|i|$$

RESULTS

Proof-of-concept Study on Microwave vs. Conventional Heating. The concept of this research work was validated by conducting comparative experiments on heating **HS** samples using microwave or conventional methods in NH_3 or N_2 atmosphere. Conventional heating of **HS** confirmed our expectation based on the literature data.[43] As shown in Figure 2**b**, Conventional heating of **HS** in flowing NH_3 significantly reduced the sample yield to below 10 wt% for 5-min heating at 1100 ºC. Replacing NH_3 with N_2 as the gas stream prevented the gasification of carbon; however, it resulted in a significant decrease in ORR activity as described in the "Effects of High-temperature Treatments on Catalytic Performance" section. In contrast, microwave heating for 5 min at designated temperatures, as shown in Figure 2**b** and Figure S5 in the Supporting Information, consistently gave higher yields than conventional heating, enabling treatment in NH_3 at 1400 ºC at a yield higher than 20 wt%. Microwave heating in NH_3 gave a higher N content in the sample than that in N_2 as shown in Figure 2**b**, accompanying a drastic increase in the ORR activity as described in the "Effects of High-temperature Treatments on Catalytic Performance" section. Similar effects were observed for **NS** samples. These data provide evidence in support of our concept, demonstrating the efficacy of selective heating of nitrogen-doped carbon in NH_3 by microwave.

Effects of High-temperature Treatment on Porous Properties and Pore Hydrophobicity. *N_2 Physisorption.* Based on literature data,[47] annealing graphene-oxide-based materials at high temperatures was initially expected to induce restacking of carbon nanosheets and eliminate micropores present between them. However, by subjecting them to short microwave heating in NH_3, nanosheet restacking was prevented, and the micropores were effectively preserved. The negligible impact of short microwave heating was evident from the N_2 adsorption isotherm data comparing **HS**, **HS-CH800**, and **HS-MW1200-NH$_3$** in Figure 3**a** for the relative pressure range below 0.01, which reveals that the N_2 uptake remains essentially the same. The BET surface areas determined for these samples were 445, 455, and 430 $m^2\ g^{-1}$, respectively, as shown in the Supporting Information. Additionally, the N_2 adsorption isotherms characterizing **NS1** and **NS2** barely changed in the low-pressure region after short microwave heating; some variations were observed at higher pressure region near $P/P_0 \sim 1$, which is attributable to gasification reactions. Notably, only the set of **HS** samples shows a step increase at $P/P_0 \sim 10^{-4}$. Plotting a semi-log derivative of N_2 isotherms, $(\partial(V_{\text{ads}})/\partial\left(\log\left(\frac{P}{P_0}\right)\right) vs. \ln(P/P_0))$, as in Figure 3**b**, identifies the first maximum corresponding to the relative pressure at which the micropore filling transition occurs and the subsequent minimum ascribed to the end of micropore filling as demonstrated in the context of crystalline microporous materials.[48] This analysis indicates that the end of micropore filling occurs at the relative pressure <0.05. Literature data, which simulate the adsorption isotherms of graphene-based materials using the grand-canonical Monte Carlo method,[49] indicate that the corresponding micropore size for $P/P_0 \sim 10^{-4}$ is approximately 1 nm. Conversely, the samples labeled with **NS**, which were synthesized by chemically reducing GO suspension using *L*-ascorbic acid in the liquid phase, barely display the characteristic step increase in N_2 uptake at the low-pressure region. The presence of these micropores seemingly results in significantly higher ORR activity for **HS** catalysts than **NS** catalysts, as described in the "Effects of High-temperature Treatments on Catalytic Performance" section, suggesting ORR proceeds within the micropores.

H_2O Vapor Adsorption. To evaluate the pore hydrophobicity of the representative samples, water vapor adsorption isotherms were collected at 25 ºC. Because the filling of N_2 molecules into the distinct micropores is characterized by the N_2 uptake at $P/P_0 \leq 0.05$ in Figure 3**a** and Figure S6 in the Supporting Information, the

micropore volume for each sample was calculated from the uptake at this relative pressure. Subsequently, these data were used to normalize the H_2O vapor adsorption data, as shown in Figure 4. **HS-CH800** demonstrates increased H_2O adsorption compared to **HS**, which is attributed to the incorporation of additional N sites facilitating H_2O adsorption, as shown by the XPS data provided in Table S1 in the Supporting Information. Microwave heating at 1200–1400 ºC increased pore hydrophobicity compared to conventional heating at 800 ºC, as shown in Figure 4 and Figure S7 in the Supporting Information. We infer that the increased pore hydrophobicity is attributed primarily to reduced N content shown in Table S1 in the Supporting Information. **NS1-CH800** exhibits a slightly higher pore hydrophobicity than **HS-MW1200-NH$_3$**, as indicated in Figure 4; however, it displays a substantially lower ORR rate compared to it, as described in the next section, once again emphasizing the crucial role of micropores in ORR catalysis.

Effects of High-temperature Treatments on Catalytic Performance. The catalytic performance for ORR in acidic electrolyte was evaluated using the rotating disc electrode apparatus. Three batches of **HS** samples gave the E_{onset} value of 0.60 ± 0.06 V vs. RHE. In addition, **HS-MW1200-NH$_3$** samples synthesized individually by two different investigators gave similar linear sweep voltammetry (LSV) curves, as shown in Figure S8 in the Supporting Information. These results indicate the reproducibility of catalyst synthesis and testing. The LSV curves in Figure 5**a** show notably higher onset potentials for **HS** catalysts than **NS** catalysts. A comparative analysis of data for **HS-CH800**, **NS1-CH800**, and **NS2-CH800** in Figure 5**a** with Figure 3 indicates that the ORR activity correlates with the micropore volume characterized by the N_2 adsorption rather than the pyridinic nitrogen content determined by XPS as shown in Figure 6 and Table S1 in the Supporting Information. This point is discussed further in the Discussion section, and these findings suggest that the reaction primarily proceeds near nitrogen sites within micropores, with minimal involvement from larger pores. The LSV data characterizing **HS**, **HS-CH800**, and **HS-CH1100** in Figure 5**a** demonstrate that heating nitrogen-doped carbon materials in NH_3 at higher temperatures enhances ORR activity. Nonetheless, the correlation between ORR activity in Figure 5**a** and pyridinic nitrogen content in Table S1 in the Supporting Information is not straightforward, as discussed in the Discussion section, implying the involvement of additional contributing factors. The LSV curve for **HS-CH1100** shows a less sharp transition from the kinetic to diffusion region than that for **HS-CH800**, as shown in Figure 5**a**. This behavior is typically associated with

the presence of internal diffusion limitations within the catalyst layer.[50] Consequently, the obtained data strongly suggest that subjecting the material to conventional heating at 1100 ºC alters its porous properties, ultimately causing mass transfer limitations. In contrast, microwave heating of **HS** in NH_3 at 1200 and 1300 ºC leads to similar LSV curves, as shown in Figure 5**a**, despite the reduced nitrogen content in the sample heated at 1300 ºC, as indicated in Figure 6 and Table S1 in the Supporting Information. Notably, this treatment preserved the sharp kinetic-to-diffusion transition region in the LSV curves in Figure 5**a**. Heating of **HS** in N_2 caused a slight decrease in the micropore volume, as shown in Figure S6 in the Supporting Information, while significantly reducing ORR activity, as indicated in Figure 5**a**. This pattern points to the imperative role of defects introduced through NH_3 etching, as discussed in the "Effects of Gas Atmosphere During Microwave Heating on Carbon Structures" and Discussion sections.[39,43,51] A similar enhancement in ORR activity is observed upon microwave heating of **NS1** in NH_3. However, it is noteworthy that the ORR activity of **NS1-MW1200-NH$_3$** remained notably lower than that of **HS**, as evidenced in Figure 5**a**, underscoring the critical importance of micropores in facilitating enhanced catalytic performance.

The Tafel slope can offer valuable insights into the rate-determining step; however, its value is influenced by many factors, such as the potential-dependent coverage of oxygenated intermediates.[52] Consequently, the value may vary significantly with applied potential, even when the rate-determining step remains the same. Hence, drawing definite conclusions from the calculated value is not always straightforward. Nevertheless, the estimated Tafel slopes for **HS-CH800** (142 mV/decade) and **HS-CH1100** (126 mV/decade) shown in Figure 5**b** are within the range of those reported for a nitrogen-doped carbon catalyst (~160 mV/decade) synthesized by pyrolyzing aniline-based polymer,[53] nitrogen- and oxygen-functionalized graphene oxide synthesized by heating an aqueous mixture of graphene oxide, urea, and hydrazine at 140 ºC (~128 mV/decade),[54] and nitrogen-doped graphene oxide synthesized by heating graphene oxide powder in NH_3 at 750 ºC (141 mV/decade).[32] These reported catalysts are characterized by rich heteroatom (N and O) contents, 8.9, 24, ~13 atomic%, respectively, which contributes to low electron conductivity[54] and their high selectivity to H_2O_2 via two-electron reduction of O_2. Hence, the comparison of the data indicates that the nature of active sites and reactive microenvironments are similar for these catalysts. In contrast, all catalysts heated by microwave at ≥1200 ºC exhibited Tafel slopes less than 100 mV/decade, as shown in Figure 5**b** and Figure

S9 in the Supporting Information. For example, the slope characterizing **HS-MW1200-NH_3** is 90 mV/decade, which is similar to the slopes of catalysts that demonstrate a high yield of H_2O.[32,54] The rate-determining step for these catalysts has been proposed to involve concerted proton and electron transfer.[54] In summary, the data indicate that microwave heating of nitrogen-doped carbon materials enhances the reaction rate towards H_2O, presumably by modifying the nature of active sites and reactive microenvironments.

Effects of Gas Atmosphere During Microwave Heating on Carbon Structures. As described in the preceding section, microwave heating of **HS** in a N_2 atmosphere at 1200 ºC led to a slight reduction in the micropore volume. However, this process retains doped nitrogen species, particularly pyridinic nitrogen content, almost the same level as that for **HS-MW1300-NH_3**, as shown in Figure 6 and Table S1 in the Supporting Information. In addition, it resulted in an increase in hydrophobicity as shown in Figure 4. Nonetheless, the catalysis data highlight a substantial decrease in the ORR rate, as indicated in Figure 5**a**. Previous studies have demonstrated that carbon materials with topological defects can act as catalysts for ORR.[27,28] In addition, it has been reported that annealing of defects in graphitic materials typically occurs between 1100 and 1500 ºC.[55] Therefore, our results imply the crucial role of defects eliminated by microwave heating of **HS** in N_2.

To characterize the extents of carbon disorders, several representative samples were characterized by Raman spectroscopy and C1s XPS. All the Raman spectra exhibit two prominent bands at approximately 1350 and 1580 cm^{-1} in Figure 7**a**, which are normally ascribed to the D_1 (or D) and G bands, respectively.[46] Notably, when **HS** was heated at 1300 ºC in NH_3 and at 1200 ºC in N_2 by microwave, distinctive G' bands emerged at approximately 2700 cm^{-1} in the resultant materials denoted as **HS-MW1300-NH_3** and **HS-MW1200-N_2**, respectively, as shown in Figure S10 in the Supporting Information. The intensity of the D_1-band is linked to the number of aromatic rings. This band becomes Raman-active only when defects, such as oxygen functional groups and topological lattice defects, are present withing the vicinity of these aromatic regions. In contrast, the intensity of the G-band is proportional to the number of sp^2-bonded carbon pairs. Additionally, the G′ band results from a combination of two phonon vibrations and serves as an indicator of long-range structural order. The two broad peaks between 1000 and 1800 cm^{-1} were deconvoluted into five bands according to a method

reported in the literature.[46] The D_3 band located at ~1500 cm^{-1} is associated with amorphous carbon and topological defects such as carbon pentagons. Therefore, the ratio of the integrated intensities of the D_3 band to the G band (I_{D_3}/I_G) was calculated from this analysis and used as a measure for the concentration of carbon defects. We consider this analysis as approximate because it is challenging to accurately fit nonlinear, significantly overlapping peaks. Nevertheless, the I_{D_3}/I_G ratio data in Figure 7**b** reveals a general decreasing trend in the concentration of defect sites at higher temperatures. Furthermore, the sample heated in N_2 (**HS-MW1200-NH_3**) exhibits a lower I_{D_3}/I_G ratio and a more pronounced G' band than the sample heated in NH_3 (**HS-MW1200-N_2**), indicating a lower concentration of carbon defects and a higher degree of structural order in **HS-MW1200-N_2**.

An increased concentration of defect sites in carbon materials has been known to broaden C1s XP spectra.[29,36,56,57] We deconvoluted each spectrum into three peaks using a method based on the literature,[57] as shown in Figure 8**a**. The first narrow peak at 284.6 eV with a full width at half maximum (FWHM) value of ~1 eV is attributed to the aromatic layers in graphitic sp^2 configurations. The second peak, broader (FWHM ≥1.5 eV) and shifted less than 1 eV from the first peak, arises from regions of defective structure. The third peak is related to π-π* levels transition, exhibiting a breadth of 4.5–5 eV and shifted by approximately 5–6 eV. Figure 8**b** also reveals a trend that aligns with the findings from Raman spectroscopy, demonstrating smaller ratios of defect peak to graphitic peak at elevated temperatures. Moreover, the data highlight distinctions between the two heating methods. Specifically, microwave heating in NH_3 leads to a higher of defects relative to conventional heating. When microwave heating is conducted in an N_2 environment, it results in a significant reduction in defect concentration compared to heating in NH_3.

Previous work has proposed that O_2 is activated at Lewis basic sites.[8] To characterize the strength of basic sites before and after microwave heating in NH_3, we used the Boehm-type titration technique.[58] The observed plateau of final pH in Figure 9, situated near neutral initial pH values, can be rationalized by the formula $0.5\ pK_a + 0.5 \log B_0 + 7$.[58] Here, pK_a denotes the value for conjugate acids of basic sites in a catalyst, and B_0 is the total moles of basic groups in the catalyst per volume of solution. The data reveal an increase in pK_a from 6.2 to 6.9 following microwave heating of **HS** in NH_3 at 1200 ºC, indicating the genesis of stronger

strength of basic sites upon microwave heating in NH_3. We postulate that the stronger basicity improves the generally weak binding strength of key surface oxygen species, such as *OH and *OOH, on metal-free carbon catalysts,[54,59] accounting partly for the enhanced activity for microwave-heated catalysts. Notably, the pK_a values characterizing the basic sites exceed the pK_a of pyridinium ion (5.2). The underlying reason for this discrepancy remains elusive. However, Herraz et al. have suggested that the presence of an amino group in the ortho-position of pyridine raises its pK_a to 6.82. In a related context, extensive research in enzyme catalysis reveals that the pK_a of an acid group buried in an enzyme's microenvironment can shift in response to the surrounding polarity and electrostatic field.[60,61] Considering the increased hydrophobicity within the micropores of **HS** after microwave heating in NH_3 at 1200 ºC, as shown in Figure 4, we infer that a more hydrophobic microenvironment near nitrogen sites destabilizes the dissociated state of protonated basic sites, thereby leading to the higher pK_a value.

DISCUSSION

Tuning Reactive Microenvironments by Short Microwave Heating. Previous studies on N-doped carbons for ORR have identified multiple factors affecting the catalyst activity, including the type and concentration of nitrogen dopants, [1,4,5,8,9,62] carbon defects,[2,27,28,63-65] pore hydrophobicity/hydrophilicity.[3,32,66] Our work highlights the crucial role of micropores and sites created through microwave heating in NH_3 for the ORR in acidic electrolytes. Specifically, our work provides evidence that the micropores, approximately 1 nm in diameter, host active sites that catalyze the ORR more efficiently than those in larger pores. This conclusion is supported by the significantly higher ORR activities for the **HS** catalysts, which possess these pores than the **NS** catalysts nearly lacking them, as shown in Figures 3 and 5. The **NS** catalysts contain a similar magnitude of concentrations of nitrogen species, especially pyridinic nitrogen, as compared to the **HS** catalysts, as indicated in Figure 6 and Table S1 in the Supporting Information. Moreover, both sets of catalysts have electrochemically accessible surface area (ECSA) values ranging from 100 to 370 $m^2\ g^{-1}$ and BET surface areas ranging from 200 to 450 $m^2\ g^{-1}$, as shown in Figures S11 and S12, respectively, in the Supporting Information. These variations in surface characteristics are insufficient to account for the significant differences in the ORR activity in Figure 5**a**. The significant role of micropore volume on ORR catalysis is

confirmed by plotting the onset potential in ORR (E_{onset}) against the micropore volume calculated from the N_2 uptake at P/P_0 = 0.05, as shown in Figure 10**a**. The limited micropore volume observed in the **NS** catalysts can be attributed to the stacking of dispersed GO during the liquid-phase reduction process. In contrast, the utilization of mild thermal reduction of GO in water, as implemented in this work and previous work,[67] minimizes the aggregation of GO. Additionally, the brief microwave heating in NH_3 maintains the micropores while simultaneously enhancing pore hydrophobicity. The Tafel slope decreased from 142 mV dec^{-1} for **HS-CH800** to 90 mV dec^{-1} for **HS-MW1200-NH$_3$**, as shown in Figure 5**b**, indicating a shift of rate-determining step or surface coverage of reacting species.[52,68] This change can be attributed to the modifications in the electrical conductivity[63], pore hydrophobic/hydrophilic properties[32], and strength of basic sites of the catalyst. The slope observed for **HS-MW1200-NH$_3$** resembles that reported for a nitrogen-doped reduced graphene oxide, possessing a relatively high electrical conductivity, as reported by McCloskey et al.[63] In their study, the investigators have proposed that the availability of electron density at the Fermi energy of the catalyst, or equivalently, its electrical conductivity, predominantly dictates whether the ORR is governed by a concerted proton-electron transfer (CPET) or an outer-sphere reduction of O_2 (aq) to O_2^- (aq), rather than the specifics of (modest) N-doping. When there exists sufficient electron density or electrical conductivity, the CPET pathway dominates due to generally lower barriers for ORR in coupled proton-electron steps compared to uncoupled steps. Our data of E_{onset} vs. pyridinic nitrogen content in Figure 10**b** demonstrate that the concentration of nitrogen content alone is insufficient to account for the variation of activity, which is consistent with their report. Notably, the slope is also close to the reported value (75 mV dec^{-1}) for the caged-NrGO catalyst reported by Nakamura et al.[32] In their work, the macroscopic caged structure generated using NaCl crystals was attributed to the pore hydrophobicity. However, our data in Figure 10**c** illustrate that the **NS1-CH800** catalyst with a high surface hydrophobicity, yet devoid of sufficient volume of micropores, shows significantly lower ORR rates than the **HS** catalysts. Therefore, we propose that their synthesis method not only yields unique macropores but also promotes the formation of micropores through the presence of small NaCl crystals between GO sheets during thermal activation. While increased hydrophobicity of the pores may reduce the potential poisoning of active sites near nitrogen-doped sites,[66] it could potentially impede proton transfer by limiting the diffusion of water. Consequently, it becomes imperative that the length of

micropores housing these sites remain sufficiently short to allow for unobstructed proton transfer. Nonetheless, a previous study has shown that hydrophobic-ordered micropores, approximately 1 nm in width, actually facilitate water transfer several orders of magnitude compared to mesopores.[69]

Significance of Microwave-assisted High-Temperature Heating in NH_3. Microwave heating of **HS** in N_2 resulted in a significant reduction in ORR activity, as indicated in Figure 5**a**, even though the resultant **HS-MW1200-N_2** contains a similar nitrogen content as compared to **HS-MW1300-NH_3**, as shown in Table S1 in the Supporting Information. These results imply that annealing in an inert atmosphere eliminates crucial sites such as pentagon carbon[28] and that nitrogen dopants alone is insufficient to achieve high ORR rates, as indicated in the literature.[2] Thus, our results emphasize the synergistic effects of nitrogen-doped sites and carbon defects, which are created through high-temperature treatment in NH_3, to catalyze ORR in acidic electrolytes efficiently. Prior investigations on atomically dispersed supported iron on N-doped carbons have shown that heat treatment in NH_3 enhances the Lewis basicity of catalysts.[70] These results align with our data in Figure 9. Previous studies have also indicated that heating carbon-black-based catalysts in NH_3 can increase their microporosity.[39] We observed similar effects of increased microporosity when utilizing phenolic resin-based carbon materials (the results not shown). However, brief heating of **HS** in NH_3 did not increase micropore volume. In summary, high-temperature heating in NH_3 proves beneficial for improving catalyst activity. Additionally, short microwave heating enables favorable modifications within micropores for ORR.

CONCLUSION

In this work, we investigated the high-temperature treatment of nitrogen-doped carbons using both conventional and microwave heating methods. We synthesized two distinct sets of samples from graphene oxides: one possessing micropores approximately 1 nm in width (**HS**) and another with fewer micropores (**NS**). These samples were subjected to heat treatments in flowing NH_3 or N_2 by the two heating techniques. Our data reveal that rapid microwave heating effectively prevents the gasification of carbon-based materials relative to conventional heating. This method allows for heating up to an average temperature of 1400 ºC in NH_3 for 5 min, yielding more than 20%. In contrast, conventional heating led to a rapid decrease in yield,

dropping below 10% at 1100 ºC. Notably, the short microwave heating of **HS** samples in NH_3 preserved their microporosity, as evidenced by N_2 sorption data, while enhancing the pore hydrophobicity, as characterized by H_2O vapor adsorption. In addition, microwave heating in NH_3 increased the strength of basic sites, as indicated by Boehm-type titration experiments. Electrochemical ORR experiments conducted in an acidic electrolyte demonstrate that **HS** catalysts heated in a NH_3 atmosphere by microwave exhibited significantly improved activity, despite reduced nitrogen content. Similarly, **NS** catalysts also exhibited increased pore hydrophobicity and enhanced ORR activity, although their activities remained notably lower than those of **HS** catalysts. Microwave heating of **HS** in a N_2 atmosphere increased pore hydrophobicity and maintained an adequate amount of nitrogen species; however, it substantially reduced ORR activity. C1s XPS data indicate that heating in N_2 reduced the concentration of defects. These findings underscore the crucial role played by the co-existence of specific nitrogen species and defects within hydrophobic micropores for achieving high ORR activity. Our study demonstrates that microwave heating in NH_3 enables us to achieve this objective. Given the significant impacts of high-temperature treatment on catalytic performance, as shown in the recent studies on atomically dispersed supported metal catalysts for ORR[71] and metal-free nitrogen-doped carbon catalysts for electrochemical reduction of CO_2, [72] our data emphasize the promising prospects of selective and fast heating by microwave to the manufacturing of improved carbon-based electrocatalysts.

FIGURES

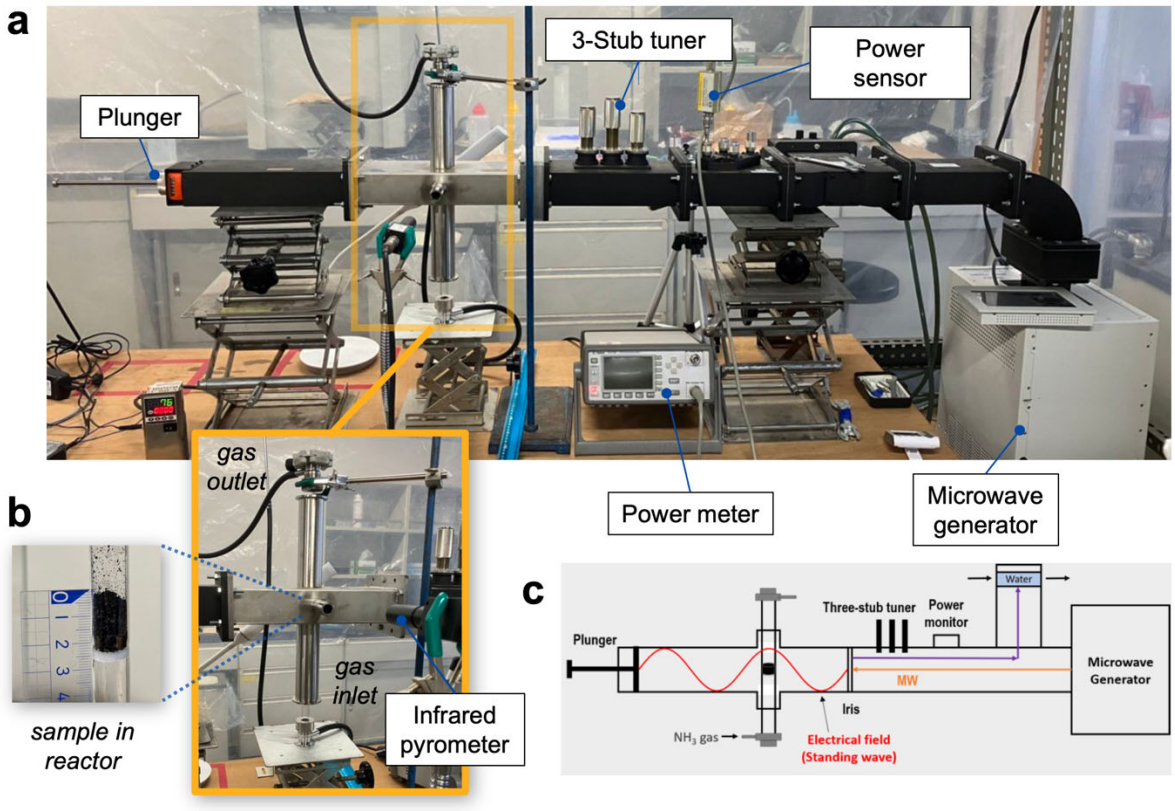

Figure 1. Photographs of the microwave applicator apparatus (**a**) a carbon sample loaded in the tubular reactor (**b**), and a simplified diagram of the microwave applicator (**c**).

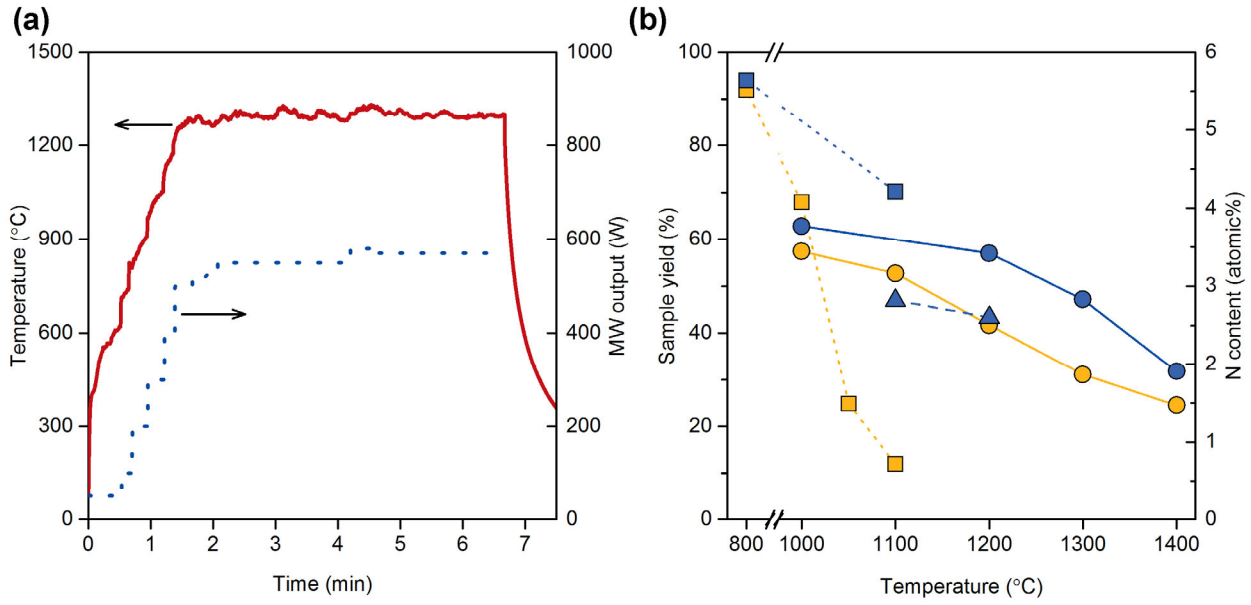

Figure 2. Microwave or conventional heating of **HS** in NH_3 or N_2: **a**, Typical temperature and microwave output profiles during heating in NH_3; **b**, Sample yield (yellow) and total nitrogen content determined by XPS (blue), for samples heated by conventional heating in NH_3 (■, dotted line) or by microwave heating in NH_3 (●, solid line) or N_2 (▲, dashed line).

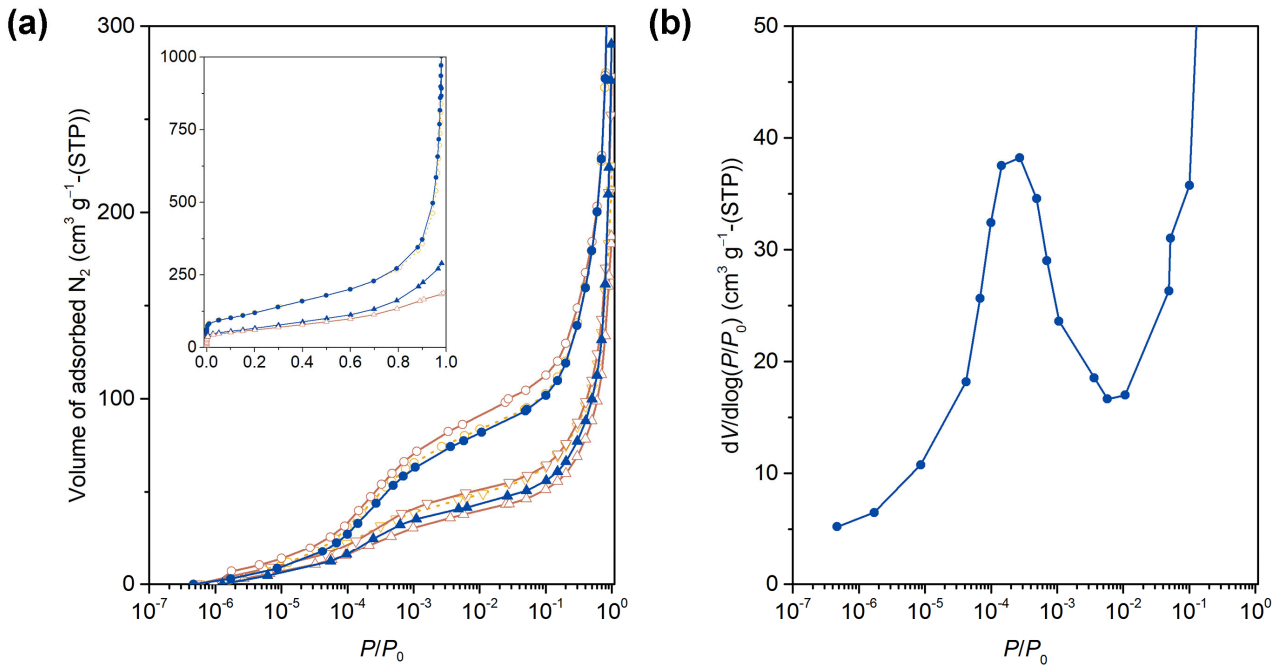

Figure 3. N_2 adsorption data: **a**, N_2 adsorption isotherms measured at 77 K on **HS** (○, yellow dotted line), **HS-CH800** (○, red solid line), **HS-MW1200-NH$_3$** (●, blue solid line), **NS1-CH800** (△, red solid line), **NS2** (▽, yellow dotted line), **NS2-CH800** (▽, red solid line), and **NS1-MW1200-NH$_3$** (▲, blue solid line). The inset shows the isotherm data characterizing **HS**, **HS-MW1200-NH$_3$**, **NS1-CH800**, and **NS1-MW1200-NH$_3$** in the linear scale; **b**, Semi-log derivative N_2 adsorption isotherms on **HS-MW1200-NH$_3$**.

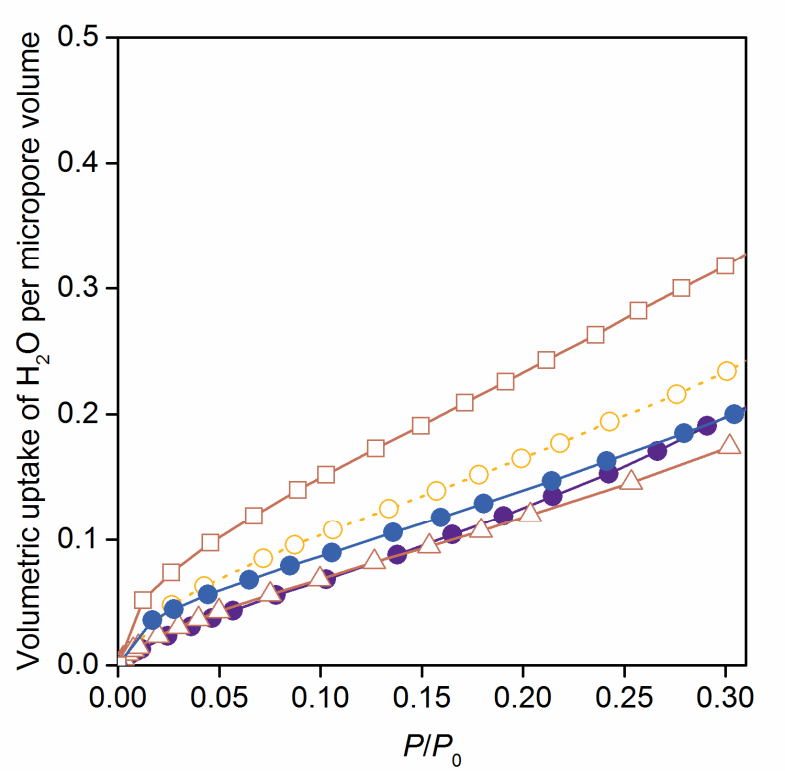

Figure 4. H_2O vapor adsorption data normalized by corresponding micropore volume calculated from N_2 uptake at $P/P_0 = 0.05$: **HS** (○, yellow dotted line), **HS-CH800** (□, red solid line), **HS-MW1200-NH$_3$** (●, blue solid line), **HS-MW1200-N$_2$** (●, purple solid line), and **NS1-CH800** (△, red solid line).

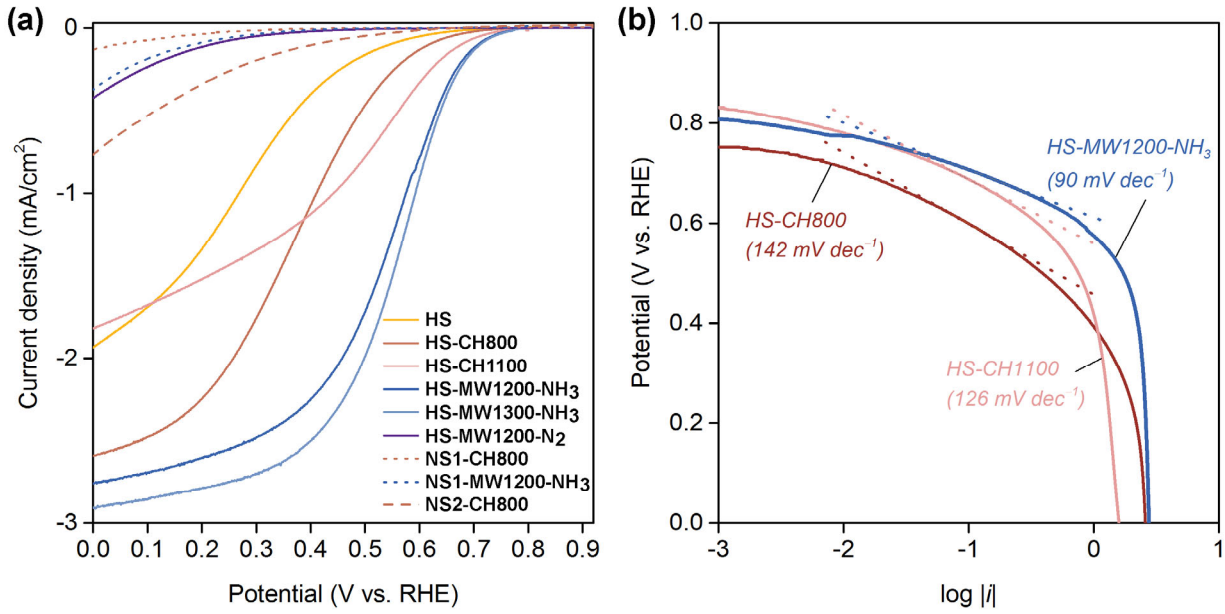

Figure 5. a, Electrochemical ORR data recorded using linear sweep voltammetry (1 mV s^{-1}) in 0.5 M H_2SO_4: **HS** (yellow line), **HS-CH800** (red line), **HS-CH1100** (light red line), **HS-MW1200-NH$_3$** (blue line), **HS-MW1300-NH$_3$** (light blue line), **HS-MW1200-N$_2$** (purple line), **NS1-CH800** (red dotted line), **NS1-MW1200-NH$_3$** (blue dotted line), and **NS2-CH800** (red dashed line); **b**, Tafel plots for **HS-CH800** (red short dashed line), **HS-CH1100** (light red short dashed line), and **HS-MW1200-NH$_3$** (blue short dashed line).

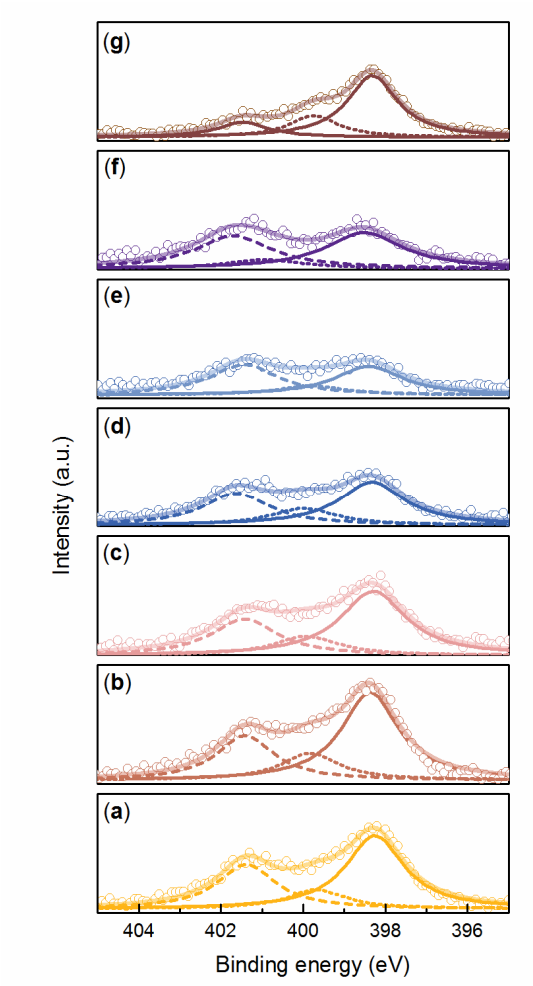

Figure 6. N1s spectra (○) and fits (line) characterizing the following samples: **a**, **HS**; **b**, **HS-CH800**; **c**, **HS-CH1100**; **d**, **HS-MW1200-NH_3**; **e**, **HS-MW1300-NH_3**; **f**, **HS-MW1200-N_2**; **g**, **NS1-CH800**. The solid, dotted, and dashed lines represent pyridinic, pyrrolic, and graphitic nitrogen species, respectively.

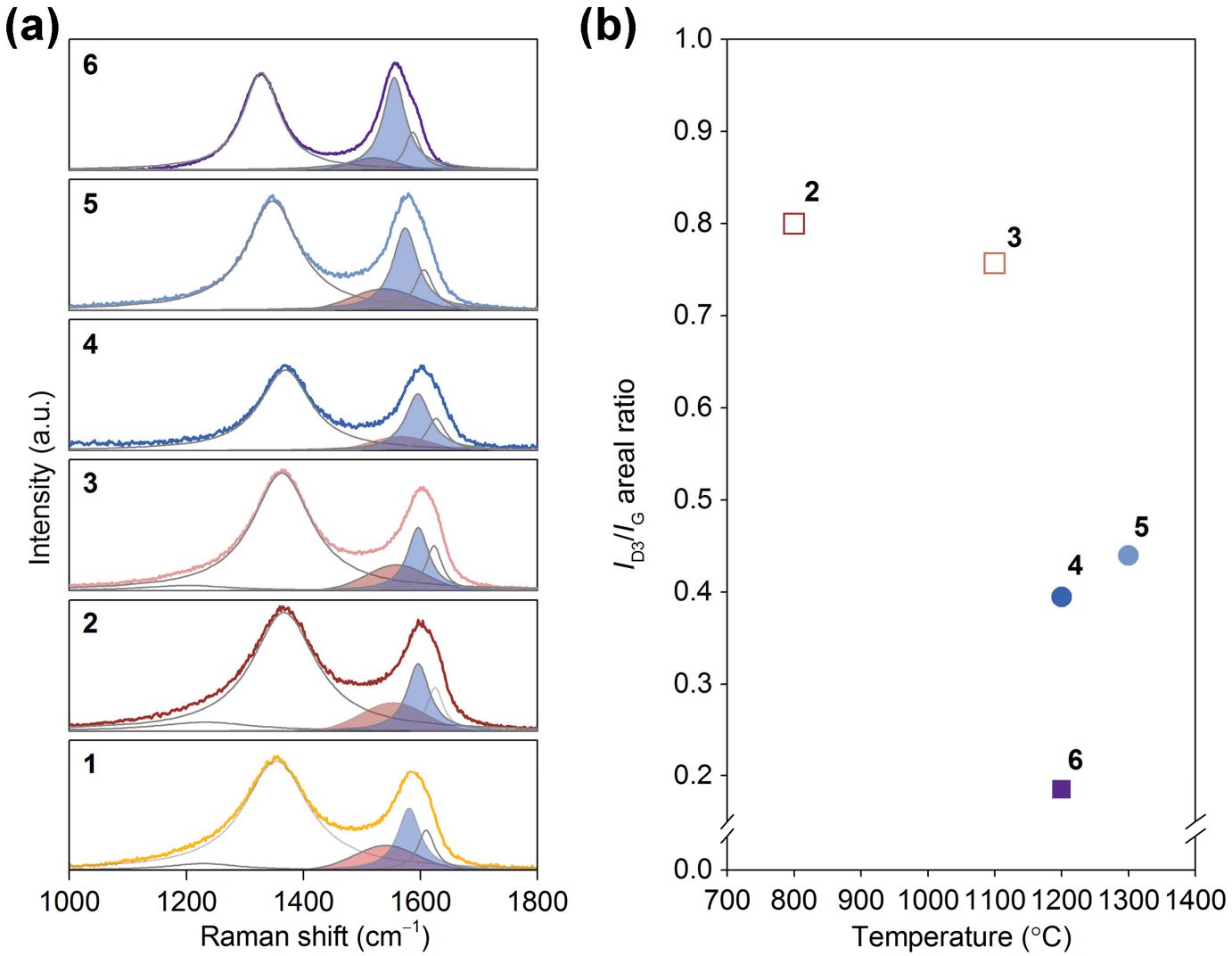

Figure 7. a, Raman spectra characterizing the following samples and spectral deconvolution: **1**, **HS** (yellow line); **2**, **HS-CH800** (red line); **3**, **HS-CH1100** (light red line); **4**, **HS-MW1200-NH$_3$** (blue line); **5**, **HS-MW1300-NH$_3$** (light blue line); **6**, **HS-MW1200-N$_2$** (purple line). The shaded peaks in red and blue represent D_3 and G peaks, respectively. **b**, Corresponding I_{D_3}/I_G areal ratio for samples **2**–**6** vs. heat treatment temperature.

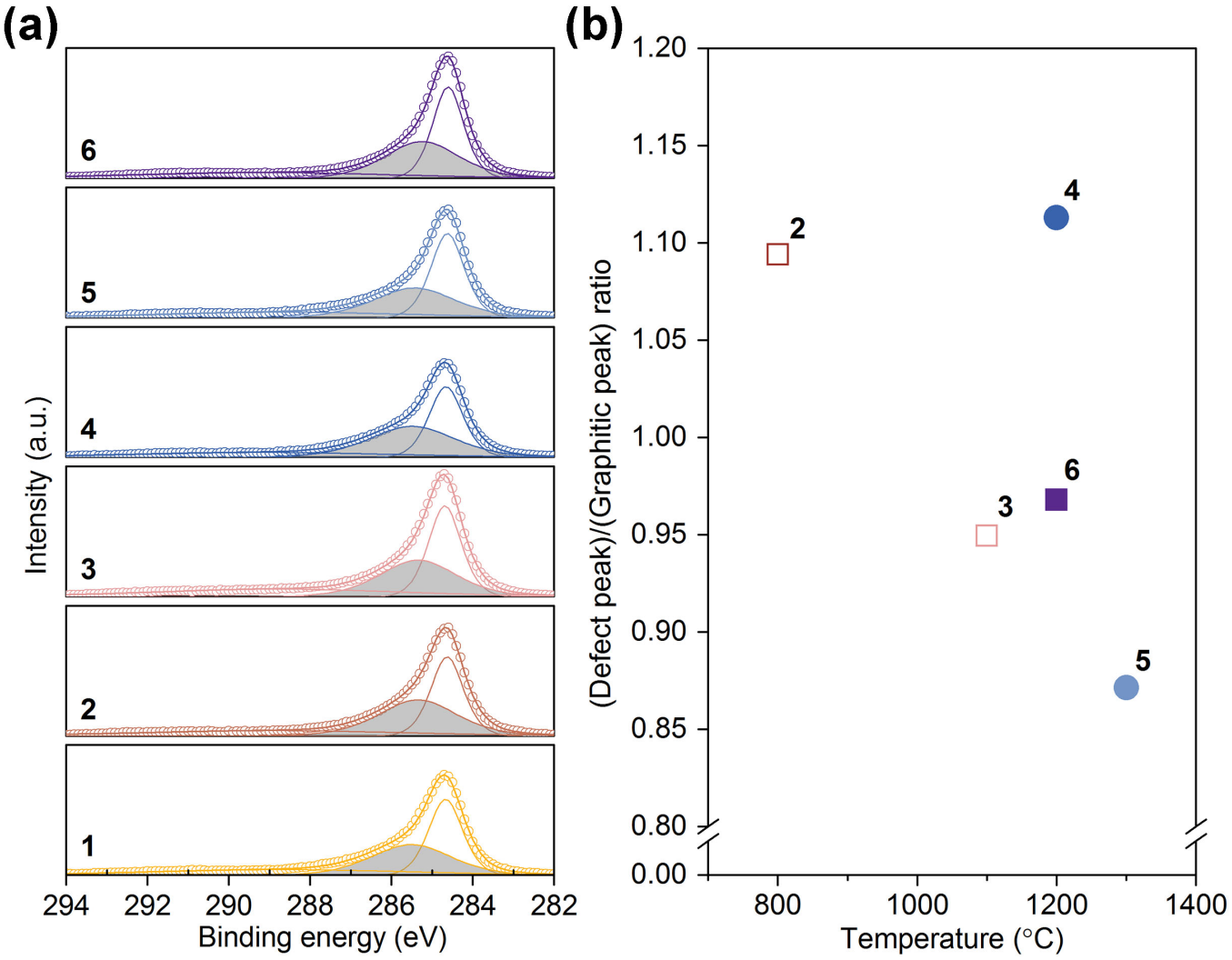

Figure 8. a, C1s spectra characterizing the following samples and spectral deconvolution: **1**, **HS** (yellow line); **2**, **HS-CH800** (red line); **3**, **HS-CH1100** (light red line); **4**, **HS-MW1200-NH_3** (blue line); **5**, **HS-MW1300-NH_3** (light blue line); **6**, **HS-MW1200-N_2** (purple line). The shaded peak represents the defect peak. **b**, Values of peak-area ratio (defect peak)/(graphitic peak) determined by the deconvolution of C1s spectra for samples **2**–**6** vs. heat treatment temperature.

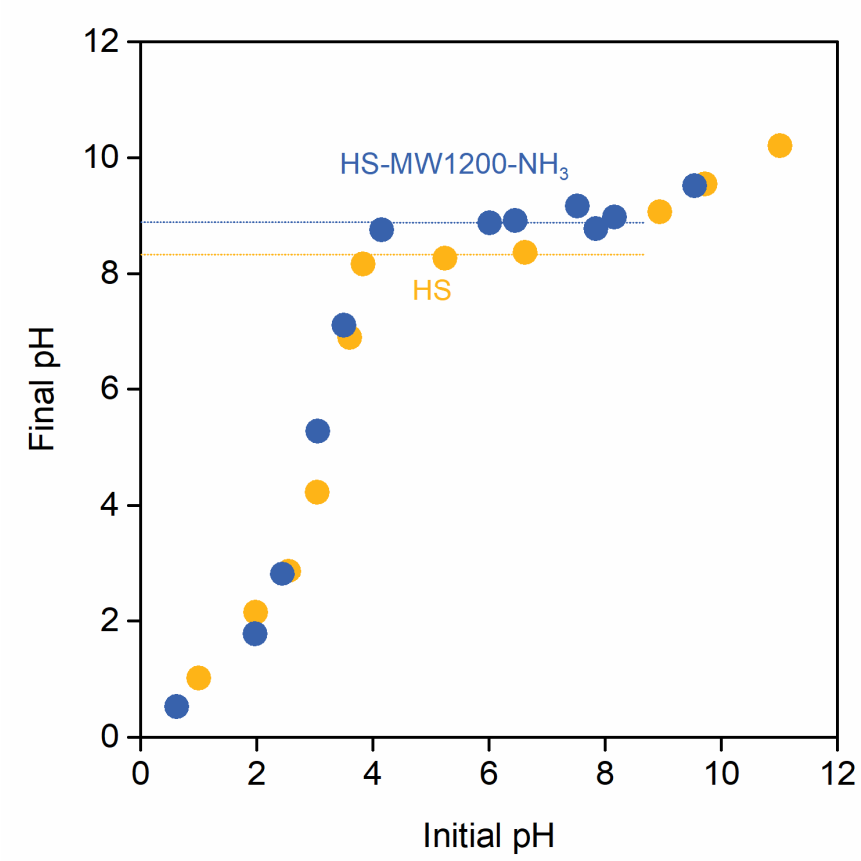

Figure 9. Boehm-type titration data characterizing **HS** and **HS-MW1200-NH$_3$**. The dotted lines represent the plateau of final pH.

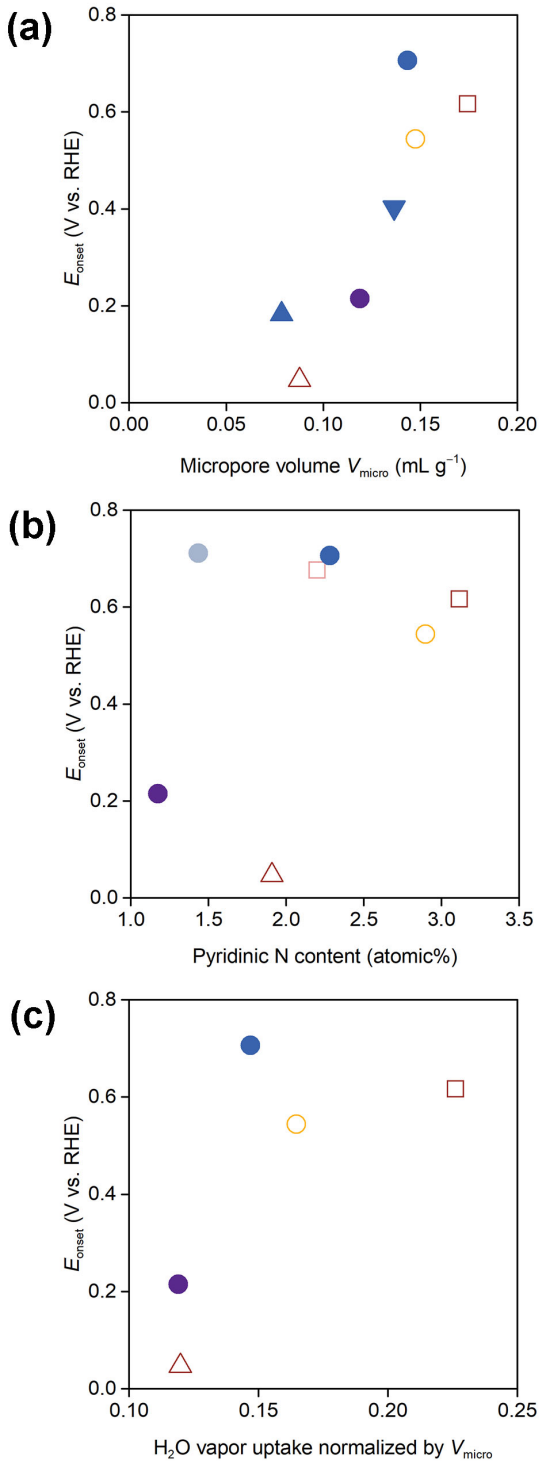

Figure 10. ORR activity (E_{onset}) plotted against the three properties catalysts (blue filled circle) **HS-MW1200-NH$_3$**, (red open square) **HS-CH800**, (yellow open circle) **HS**, (filled downward-pointing triangle) **NS2-CH800**, (purple filled circle) **HS-MW1200-N$_2$**, (blue filled triangle) **NS1- MW1200-NH$_3$**, (red open triangle) **NS1-CH800**, (light blue filled circle) **HS-MW1300-NH$_3$**, (light red open square) **HS-CH1100**: **a**, micropore volume (V_{micro}) calculated from the N_2 uptake at $P/P_0 = 0.05$ by converting adsorbed gas volumes (cm^3 $gcat^{-1}$ at STP) to liquid volumes using a density conversion factor (0.029 mol cm^{-3} for N_2); **b**, pyridinic nitrogen content quantified by XPS; **c**, H_2O vapor uptake at $P/P_0 = 0.20$ normalized by V_{micro}.

ASSOCIATED CONTENT

Supporting Information. Synthesis scheme of nitrogen-doped catalysts. SEM images of **NS1**, **NS2**, and **HS** samples. A photograph of **HS** sample. Apparatus used for conventional heating experiments. Calibration of the IR pyrometer using a carbon sample. Temperature profiles during microwave heating of **HS** samples in NH_3 at 1000, 1200, 1300, or 1400 ºC. Nitrogen content quantified by N1s XPS. N_2 adsorption isotherms measured at 77 K. H_2O vapor adsorption data measured at 25 ºC. LSV curves. Tafel plots. Raman spectra. Measurements of electrochemically accessible surface area (ECSA). BET surface area and ECSA data. This material is available free of charge via the Internet at http://pubs.acs.org.

AUTHOR INFORMATION

Corresponding Author

*iogino@eng.hokudai.ac.jp

Author Contributions

The manuscript was written through contributions of all authors. All authors have given approval to the final version of the manuscript.

Present Addresses

†Advanced Institute for Materials Research, Tohoku University, Sendai, Miyagi 980-8577, Japan

Funding Sources

This work has been supported partially by Tanigawa Promotion Foundation for Thermal Technology, Iketani Science and Technology Foundation, and Adaptable and Seamless Technology Transfer Program through Target-driven R&D (A-STEP) from Japan Science and Technology Agency (JST).

ACKNOWLEDGMENT

We acknowledge Daichi Homma at Hokkaido University for his help in the Boehm-type titration experiments, Takuya Ikka, Yuya Yokoyama, and Kohei Kitano at Hokkaido University for helpful discussion on the synthesis of **HS**, Masahiro Imai for helpful discussion on high-resolution N_2 adsorption experiments, and Prof. Keiichiro Kashimura at Chubu University for his help in the single-mode microwave apparatus and helpful discussion on microwave heating. We also acknowledge Shunsuke Kamatari, Go Fukazawa, Konosuke Minakami, and Hikaru Sugata at Hokkaido University for fruitful discussion on microwave heating of carbon materials. A part of this work was conducted at Joint-use Facilities: Laboratory of Nano-Micro Material Analysis, Hokkaido University, supported by Nano-technology Platform Program of the Ministry of Education, Culture, Sports, Science and Technology (MEXT), Japan.

ABBREVIATIONS

CH, conventional heating; MW, microwave

REFERENCES

(1) Matter, P. H.; Zhang, L.; Ozkan, U. S. The Role of Nanostructure in Nitrogen-containing Carbon Catalysts for the Oxygen Reduction Reaction *J. Catal.* **2006**, *239*, 83–96.

(2) Jiang, L.; van Dijk, B.; Wu, L.; Maheu, C.; Hofmann, J. P.; Tudor, V.; Koper, M. T. M.; Hetterscheid, D. G. H.; Schneider, G. F. Predoped Oxygenated Defects Activate Nitrogen-Doped Graphene for the Oxygen Reduction Reaction *ACS Catal* **2022**, *12*, 173–182.

(3) Seredych, M.; Szczurek, A.; Fierro, V.; Celzard, A.; Bandosz, T. J. Electrochemical Reduction of Oxygen on Hydrophobic Ultramicroporous PolyHIPE Carbon *ACS Catal.* **2016**, *6*, 5618-5628.

(4) Ikeda, T.; Boero, M.; Huang, S.-F.; Terakura, K.; Oshima, M.; Ozaki, J.-i. Carbon Alloy Catalysts: Active Sites for Oxygen Reduction Reaction *J. Phys. Chem. C* **2008**, *112*, 14706–14709.

(5) Liu, G.; Li, X.; Ganesan, P.; Popov, B. N. Studies of Oxygen Reduction Reaction Active Sites and Stability of Nitrogen-Modified Carbon Composite Catalysts for PEM Fuel Cells *Electrochim. Acta* **2010**, *55*, 2853–2858.

(6) Wei, W.; Liang, H.; Parvez, K.; Zhuang, X.; Feng, X.; Mullen, K. Nitrogen-Doped Carbon Nanosheets with Size-Defined Mesopores as Highly Efficient Metal-Free Catalyst for the Oxygen Reduction Reaction *Angew. Chem. Int. Ed.* **2014**, *53*, 1570–1574.

(7) Shui, J.; Wang, M.; Du, F.; Dai, L. N-Doped Carbon Nanomaterials are Durable Catalysts for Oxygen Reduction Reaction in Acidic Fuel Cells *Science Adv.* **2015**, *1*, e1400129.

(8) Guo, D.; Shibuya, R.; Akiba, C.; Saji, S.; Kondo, T.; Nakamura, J. Active Sites of Nitrogen-Doped Carbon Materials for Oxygen Reduction Reaction Clarified Using Model Catalysts *Science* **2016**, *351*, 361–365.

(9) Mamtani, K.; Jain, D.; Zemlyanov, D.; Celik, G.; Luthman, J.; Renkes, G.; Co, A. C.; Ozkan, U. S. Probing the Oxygen Reduction Reaction Active Sites over Nitrogen-Doped Carbon Nanostructures (CNx) in Acidic Media Using Phosphate Anion *ACS Catal.* **2016**, *6*, 7249–7259.

(10) Quílez-Bermejo, J.; Morallón, E.; Cazorla-Amorós, D. Metal-Free Heteroatom-Doped Carbon-Based Catalysts for ORR: A Critical Assessment about the Role of Heteroatoms *Carbon* **2020**, *165*, 434–454.

(11) Zhai, Q.; Pan, Y.; Dai, L. Carbon-Based Metal-Free Electrocatalysts: Past, Present, and Future *Acc. Mater. Res.* **2021**, *2*, 1239–1250.

(12) Asset, T.; Maillard, F.; Jaouen, F. *Supported Metal Single Atom Catalysis* **2022**, 531–582.

(13) Chen, M.; He, Y.; Spendelow, J. S.; Wu, G. Atomically Dispersed Metal Catalysts for Oxygen Reduction *ACS Energy Lett.* **2019**, *4*, 1619–1633.

(14) Chung, H. T.; Cullen, D. A.; Higgins, D.; Sneed, B. T.; Holby, E. F.; More, K. L.; Zelenay, P. Direct Atomic-Level Insight into the Active Sites of a High-Performance PGM-Free ORR Catalyst *Science* **2017**, *357*, 479–484.

(15) Wang, Y.; Mao, J.; Meng, X.; Yu, L.; Deng, D.; Bao, X. Catalysis with Two-Dimensional Materials Confining Single Atoms: Concept, Design, and Applications *Chem Rev* **2019**, *119*, 1806–1854.

(16) Xie, J.; Kammert, J. D.; Kaylor, N.; Zheng, J. W.; Choi, E.; Pham, H. N.; Sang, X.; Stavitski, E.; Attenkofer, K.; Unocic, R. R.; Datye, A. K.; Davis, R. J. Atomically Dispersed Co and Cu on N-Doped Carbon for Reactions Involving C–H Activation *ACS Catal.* **2018**, *8*, 3875–3884.

(17) Arrigo, R.; Schuster, M. E.; Xie, Z.; Yi, Y.; Wowsnick, G.; Sun, L. L.; Hermann, K. E.; Friedrich, M.; Kast, P.; Hävecker, M.; Knop-Gericke, A.; Schlögl, R. Nature of the N–Pd Interaction in Nitrogen-Doped Carbon Nanotube Catalysts *ACS Catal.* **2015**, *5*, 2740–2753.

(18) He, L.; Weniger, F.; Neumann, H.; Beller, M. Synthesis, Characterization, and Application of Metal Nanoparticles Supported on Nitrogen-Doped Carbon: Catalysis beyond Electrochemistry *Angew. Chem. Int. Ed.* **2016**, *55*, 12582–12594.

(19) Shi, W.; Wu, K.-H.; Xu, J.; Zhang, Q.; Zhang, B.; Su, D. S. Enhanced Stability of Immobilized Platinum Nanoparticles through Nitrogen Heteroatoms on Doped Carbon Supports *Chem. Mater.* **2017**, *29*, 8670–8678.

(20) Rahman, F. B. A.; Tien, H. N.; Colon-Mercado, H.; Ganesan, P.; Elvington, M. C.; Gaillard, J. B.; Karakalos, S. G.; Regalbuto, J. R. Stabilization of Ultrasmall Platinum Nanoparticles by Nitrogen-Doped Carbon: Implications for Catalysis and Electrocatalysis *ACS Appl. Nano Mater.* **2022**, *5*, 10292–10302.

(21) Pulikkal Thumbayil, R.; Christensen, D. B.; Mielby, J.; Kegnæs, S. Dehydrogenation of Bioethanol Using Cu Nanoparticles Supported on N-Doped Ordered Mesoporous Carbon *ChemCatChem* **2020**, *12*, 5644–5655.

(22) Jansen, R. J. J.; van Bekkum, H. Amination and Ammoxidation of Activated Carbons *Carbon* **1994**, *32*, 1507–1516.

(23) Kundu, S.; Xia, W.; Busser, W.; Becker, M.; Schmidt, D. A.; Havenith, M.; Muhler, M. The Formation of Nitrogen-Containing Functional Groups on Carbon Nanotube Surfaces: a Quantitative XPS and TPD Study *Phys. Chem. Chem. Phys.* **2010**, *12*, 4351–4359.

(24) Li, X.; Wang, H.; Robinson, J. T.; Sanchez, H.; Diankov, G.; Dai, H. Simultaneous Nitrogen Doping and Reduction of Graphene Oxide *J. Am. Chem. Soc.* **2009**, *131*, 15939–15944.

(25) Arrigo, R.; Hävecker, M.; Wrabetz, S.; Blume, R.; Lerch, M.; McGregor, J.; Parrott, E. P. J.; Zeitler, J. A.; Gladden, L. F.; Knop-Gericke, A.; Schlögl, R.; Su, D. S. Tuning the Acid/Base Properties of Nanocarbons by Functionalization via Amination *J. Am. Chem. Soc.* **2010**, *132*, 9616–9630.

(26) Arrigo, R.; Hävecker, M.; Schlögl, R.; Su, D. S. Dynamic Surface Rearrangement and Thermal Stability of Nitrogen Functional Groups on Carbon Nanotubes *Chem. Commun.* **2008**, 4891–4893.

(27) Wang, X.; Jia, Y.; Mao, X.; Zhang, L.; Liu, D.; Song, L.; Yan, X.; Chen, J.; Yang, D.; Zhou, J.; Wang, K.; Du, A.; Yao, X. A Directional Synthesis for Topological Defect in Carbon *Chem* **2020**, *6*, 2009–2023.

(28) Qu, Y.; Li, Z.; Chen, W.; Lin, Y.; Yuan, T.; Yang, Z.; Zhao, C.; Wang, J.; Zhao, C.; Wang, X.; Zhou, F.; Zhuang, Z.; Wu, Y.; Li, Y. Identification of Active Sites for Acidic Oxygen Reduction on Carbon Catalysts with and without Nitrogen Doping *Nat. Catal.* **2018**, *1*, 781–786.

(29) Darmstadt, H.; Roy, C. Surface Spectroscopic Study of Basic Sites on Carbon Blacks *Carbon* **2003**, *41*, 2662–2665.

(30) Friedel Ortega, K.; Arrigo, R.; Frank, B.; Schlögl, R.; Trunschke, A. Acid–Base Properties of N-Doped Carbon Nanotubes: A Combined Temperature-Programmed Desorption, X-ray Photoelectron Spectroscopy, and 2-Propanol Reaction Investigation *Chem. Mater.* **2016**, *28*, 6826–6839.

(31) Bera, B.; Chakraborty, A.; Kar, T.; Leuaa, P.; Neergat, M. Density of States, Carrier Concentration, and Flat Band Potential Derived from Electrochemical Impedance Measurements of N-Doped Carbon and Their Influence on Electrocatalysis of Oxygen Reduction Reaction *J. Phys. Chem. C* **2017**, *121*, 20850-20856.

(32) Singh, S. K.; Takeyasu, K.; Homma, K.; Ito, S.; Morinaga, T.; Endo, Y.; Furukawa, M.; Mori, T.; Ogasawara, H.; Nakamura, J. Activating Nitrogen-doped Graphene Oxygen Reduction Electrocatalysts in Acidic Electrolytes using Hydrophobic Cavities and Proton-conductive Particles *Angew. Chem. Int. Ed.* **2022**, *61*, e202212506.

(33) Fu, S.; Li, M.; de Jong, W.; Kortlever, R. Tuning the Properties of N-Doped Biochar for Selective CO_2 Electroreduction to CO *ACS Catal.* **2023**, *13*, 10309–10323.

(34) Pope, M. A.; Aksay, I. A. Four-Fold Increase in the Intrinsic Capacitance of Graphene through Functionalization and Lattice Disorder *J. Phys. Chem. C* **2015**, *119*, 20369–20378.

(35) Mattevi, C.; Eda, G.; Agnoli, S.; Miller, S.; Mkhoyan, K. A.; Celik, O.; Mastrogiovanni, D.; Granozzi, G.; Garfunkel, E.; Chhowalla, M. Evolution of Electrical, Chemical, and Structural Properties of Transparent and Conducting Chemically Derived Graphene Thin Films *Adv. Funct. Mater.* **2009**, *19*, 2577–2583.

(36) Maldonado, S.; Morin, S.; Stevenson, K. J. Structure, Composition, and Chemical Reactivity of Carbon Nanotubes by Selective Nitrogen Doping *Carbon* **2006**, *44*, 1429–1437.

(37) Boehm, H. P.; Mair, G.; Stoehr, T.; De Rincón, A. R.; Tereczki, B. Carbon as a Catalyst in Oxidation Reactions and Hydrogen Halide Elimination Reactions *Fuel* **1984**, *63*, 1061–1063.

(38) Johnson, G. E.; Decker, W. A.; Forney, A. J.; Field, J. H. Hydrogen Cyanide Produced from Coal and Ammonia *Ind. Eng. Chem. Process Des. Dev.* **1968**, *7*, 137–143.

(39) Jaouen, F.; Lefèvre, M.; Dodelet, J.-P.; Cai, M. Heat-Treated Fe/N/C Catalysts for O_2 Electroreduction: Are Active Sites Hosted in Micropores? *J. Phys. Chem. B* **2006**, *110*, 5553–5558.

(40) Charreteur, F.; Jaouen, F.; Ruggeri, S.; Dodelet, J.-P. Fe/N/C Non-Precious Catalysts for PEM Fuel Cells: Influence of the Structural Parameters of Pristine Commercial Carbon Blacks on their Activity for Oxygen Reduction *Electrochim. Acta* **2008**, *53*, 2925–2938.

(41) Koslowski, U.; Herrmann, I.; Bogdanoff, P.; Barkschat, C.; Fiechter, S.; Iwata, N.; Takahashi, H.; Nishikori, H. Evaluation and Analysis of PEM-FC Performance using Non-Platinum Cathode Catalysts based on Pyrolysed Fe- and Co-Porphyrins - Influence of a Secondary Heat-treatment *ECS Transactions* **2008**, *13*, 125.

(42) Li, J.; Sougrati, M. T.; Zitolo, A.; Ablett, J. M.; Oğuz, I. C.; Mineva, T.; Matanovic, I.; Atanassov, P.; Huang, Y.; Zenyuk, I.; Di Cicco, A.; Kumar, K.; Dubau, L.; Maillard, F.; Dražić, G.; Jaouen, F. Identification of Durable and Non-Durable FeN_x Sites in Fe–N–C Materials for Proton Exchange Membrane Fuel Cells *Nat. Catal.* **2020**, *4*, 10–19.

(43) Jaouen, F.; Charreteur, F.; Dodelet, J. P. *J.* Fe-Based Catalysts for Oxygen Reduction in PEMFCs: Importance of the Disordered Phase of the Carbon Support *J. Electrochem. Soc.* **2006**, *153*, A689.

(44) Horikoshi, S.; Osawa, A.; Sakamoto, S.; Serpone, N. Control of microwave-generated hot spots. Part V. Mechanisms of hot-spot generation and aggregation of catalyst in a microwave-assisted reaction in toluene catalyzed by Pd-loaded AC particulates *Appl. Catal. A: Gen.* **2013**, *460–461*, 52–60.

(45) Ramirez, A.; Hueso, J. L.; Abian, M.; Alzueta, M. U.; Mallada, R.; Santamaria, J. Escaping Undesired Gas-Phase Chemistry: Microwave-Driven Selectivity Enhancement in Heterogeneous Catalytic Reactors *Science Adv.* **2019**, *5*, eaau9000.

(46) Sadezky, A.; Muckenhuber, H.; Grothe, H.; Niessner, R.; Pöschl, U. Raman Microspectroscopy of Soot and Related Carbonaceous Materials: Spectral Analysis and Structural Information. *Carbon* **2005**, *43*, 1731–1742.

(47) Worsley, M. A.; Pham, T. T.; Yan, A.; Shin, S. J.; Lee, J. R. I.; Bagge-Hansen, M.; Mickelson, W.; Zettl, A., Synthesis and Characterization of Highly Crystalline Graphene Aerogels. *ACS Nano* **2014,** *8*, 11013–11022.

(48) Borghard, W. S.; Reischman, P. T.; Sheppard, E. W. Argon Sorption in ZSM-5 *J. Catal.* **1993**, *139*, 19–23.

(49) Kowalczyk, P.; Gauden, P. A.; Furmaniak, S.; Terzyk, A. P.; Wiśniewski, M.; Ilnicka, A.; Łukaszewicz, J.; Burian, A.; Włoch, J.; Neimark, A. V. Morphologically Disordered Pore Model for Characterization of Micro-mesoporous Carbons *Carbon* **2017**, *111*, 358–370.

(50) Dix, S. T.; Lu, S.; Linic, S. Critical Practices in Rigorously Assessing the Inherent Activity of Nanoparticle Electrocatalysts *ACS Catal.* **2020**, *10*, 10735–10741.

(51) Li, C.; Wang, Y.; Xiao, N.; Li, H.; Ji, Y.; Guo, Z.; Liu, C.; Qiu, J. Nitrogen-Doped Porous Carbon from Coal for High Efficiency CO_2 Electrocatalytic Reduction *Carbon* **2019**, *151*, 46–52.

(52) Holewinski, A.; Linic, S. Elementary Mechanisms in Electrocatalysis: Revisiting the ORR Tafel Slope *J. Electrochem. Soc.* **2012**, *159*, H864–H870.

(53) Luo, F.; Wagner, S.; Onishi, I.; Selve, S.; Li, S.; Ju, W.; Wang, H.; Steinberg, J.; Thomas, A.; Kramm, U. I.; Strasser, P. Surface Site Density and Utilization of Platinum Group Metal (PGM)-free Fe–NC and FeNi–NC Electrocatalysts for the Oxygen Reduction Reaction *Chem. Sci.* **2021**, *12*, 384–396.

(54) Kim, H. W.; Bukas, V. J.; Park, H.; Park, S.; Diederichsen, K. M.; Lim, J.; Cho, Y. H.; Kim, J.; Kim, W.; Han, T. H.; Voss, J.; Luntz, A. C.; McCloskey, B. D. Mechanisms of Two-Electron and Four-Electron Electrochemical Oxygen Reduction Reactions at Nitrogen-Doped Reduced Graphene Oxide *ACS Catal.* **2019**, *10*, 852–863.

(55) Campos-Delgado, J.; Kim, Y. A.; Hayashi, T.; Morelos-Gómez, A.; Hofmann, M.; Muramatsu, H.; Endo, M.; Terrones, H.; Shull, R. D.; Dresselhaus, M. S.; Terrones, M., Thermal Stability Studies of CVD-grown Graphene Nanoribbons: Defect Annealing and Loop Formation. *Chem. Phys. Lett.* **2009,** *469*, 177–182.

(56) Takahagi, T.; Ishitani, A. XPS Study on the Surface Structure of Carbon Fibers Using Chemical Modification and C1s Line Shape Analysis *Carbon* **1988**, *26*, 389–395.

(57) Estrade-Szwarckopf, H. XPS Photoemission in Carbonaceous Materials: A "Defect" Peak Beside the Graphitic Asymmetric Peak. *Carbon* **2004**, *42*, 1713–1721.

(58) Herranz, J.; Jaouen, F.; Lefèvre, M.; Kramm, U. I.; Proietti, E.; Dodelet, J.-P.; Bogdanoff, P.; Fiechter, S.; Abs-Wurmbach, I.; Bertrand, P.; Arruda, T. M.; Mukerjee, S. Unveiling N-Protonation and Anion-Binding Efects on Fe/N/C-Catalysts for O_2 Reduction in PEM Fuel Cells *J. Phys. Chem. C* **2011**, *115*, 16087–16097.

(59) Kulkarni, A.; Siahrostami, S.; Patel, A.; Nørskov, J. K. Understanding Catalytic Activity Trends in the Oxygen Reduction Reaction. *Chem. Rev.* **2018**, *118* (5), 2302–2312

(60) Isom, D. G.; Castaneda, C. A.; Cannon, B. R.; Garcia-Moreno, B. Large Shifts in pK_a Values of Lysine Residues Buried Inside a Protein. *Proc. Natl. Acad. Sci. U.S.A.* **2011**, *108*, 5260–5265.

(61) Fried, S. D.; Boxer, S. G. Electric Fields and Enzyme Catalysis. *Annu. Rev. Biochem* **2017**, *86*, 387–415.

(62) Wang, T.; Chen, Z.-X.; Chen, Y.-G.; Yang, L.-J.; Yang, X.-D.; Ye, J.-Y.; Xia, H.-P.; Zhou, Z.-Y.; Sun, S.-G. Identifying the Active Site of N-Doped Graphene for Oxygen Reduction by Selective Chemical Modification *ACS Energy Letters* **2018**, *3*, 986–991.

(63) Kim, H. W.; Park, H.; Roh, J. S.; Shin, J. E.; Lee, T. H.; Zhang, L.; Cho, Y. H.; Yoon, H. W.; Bukas, V. J.; Guo, J.; Park, H. B.; Han, T. H.; McCloskey, B. D. Carbon Defect Characterization of Nitrogen-Doped Reduced Graphene Oxide Electrocatalysts for the Two-Electron Oxygen Reduction Reaction *Chem. Mater.* **2019**, *31*, 3967–3973.

(64) Jiang, Y.; Yang, L.; Sun, T.; Zhao, J.; Lyu, Z.; Zhuo, O.; Wang, X.; Wu, Q.; Ma, J.; Hu, Z. Significant Contribution of Intrinsic Carbon Defects to Oxygen Reduction Activity *ACS Catal.* **2015**, *5*, 6707–6712.

(65) Stamatin, S. N.; Hussainova, I.; Ivanov, R.; Colavita, P. E. Quantifying Graphitic Edge Exposure in Graphene-Based Materials and Its Role in Oxygen Reduction Reactions *ACS Catal.* **2016**, *6*, 5215–5221.

(66) Takeyasu, K.; Furukawa, M.; Shimoyama, Y.; Singh, S. K.; Nakamura, J. Role of Pyridinic Nitrogen in the Mechanism of the Oxygen Reduction Reaction on Carbon Electrocatalysts *Angew. Chem. Int. Ed.* **2021**, *60*, 5121–5124.

(67) Kim, H. W.; Ross, M. B.; Kornienko, N.; Zhang, L.; Guo, J.; Yang, P.; McCloskey, B. D. Efficient Hydrogen Peroxide Generation Using Reduced Graphene Oxide-Based Oxygen Reduction Electrocatalysts *Nat. Catal.* **2018**, *1*, 282–290.

(68) Shinagawa, T.; Garcia-Esparza, A. T.; Takanabe, K. Insight on Tafel Slopes from a Microkinetic Analysis of Aqueous Electrocatalysis for Energy Conversion *Sci Rep* **2015**, *5*, 13801.

(69) Radha, B.; Esfandiar, A.; Wang, F. C.; Rooney, A. P.; Gopinadhan, K.; Keerthi, A.; Mishchenko, A.; Janardanan, A.; Blake, P.; Fumagalli, L.; Lozada-Hidalgo, M.; Garaj, S.; Haigh, S. J.; Grigorieva, I. V.; Wu, H. A.; Geim, A. K. Molecular Transport through Capillaries Made with Atomic-Scale Precision *Nature* **2016**, *538*, 222–225.

(70) Zitolo, A.; Goellner, V.; Armel, V.; Sougrati, M. T.; Mineva, T.; Stievano, L.; Fonda, E.; Jaouen, F. Identification of Catalytic Sites for Oxygen Reduction in Iron- and Nitrogen-doped Graphene Materials. *Nat. Mater.* **2015**, *14*, 937–942.

(71) Zachman, M. J.; Cullen, D. A.; Hermann, R. P.; Alp, E. E.; Lavina, B.; Karakalos, S.; Lucero, M.; Zhang, B.; Wang, M.; Feng, Z.; Wang, G.; Xie, J.; Myers, D. J.; Dodelet, J.-P.; Wu, G. Tuning the Thermal Activation Atmosphere Breaks the Activity–Stability Trade-off of Fe–N–C Oxygen Reduction Fuel Cell Catalysts. *Nat. Catal.* **2023**, *6*, 1215–1227.

(72) Daiyan, R.; Tan, X.; Chen, R.; Saputera, W. H.; Tahini, H. A.; Lovell, E.; Ng, Y. H.; Smith, S. C.; Dai, L.; Lu, X.; Amal, R. Electroreduction of CO_2 to CO on a Mesoporous Carbon Catalyst with Progressively Removed Nitrogen Moieties *ACS Energy Lett.* **2018**, *3*, 2292–2298.

TOC graphic